Title
About the Compatibility between High Voltage Spinel Cathode Materials and Solid Oxide Electrolytes as a Function of Temperature

Journal
ACS Applied Materials & Interfaces, 8(40)

ISSN
1944-8244

Authors
Miara, Lincoln
Windmüller, Anna
Tsai, Chih-Long
et al.

Publication Date
2016-10-12

DOI
10.1021/acsami.6b09059

Peer reviewed

ACS APPLIED MATERIALS & INTERFACES

Research Article

www.acsami.org

About the Compatibility between High Voltage Spinel Cathode Materials and Solid Oxide Electrolytes as a Function of Temperature

Lincoln Miara,[*,†] Anna Windmüller,[‡,∥] Chih-Long Tsai,[‡,∥] William D. Richards,[§] Qianli Ma,[‡,∥] Sven Uhlenbruck,[‡,∥] Olivier Guillon,[‡,∥] and Gerbrand Ceder[§,⊥]

[†]Samsung Advanced Institute of Technology − USA, 255 Main Street, Suite 702, Cambridge, Massachusetts 02142, United States

[‡]Institute of Energy and Climate Research, Materials Synthesis and Processing (IEK-1), Forschungszentrum Jülich GmbH, 52425 Jülich, Germany

[§]Department of Materials Science and Engineering, Massachusetts Institute of Technology, 77 Massachusetts Avenue, Cambridge, Massachusetts 02139, United States

[∥]Jülich Aachen Research Alliance: JARA-Energy, Forschungszentrum Jülich GmbH, 52425 Jülich, Germany

[⊥]Department of Materials Science and Engineering, UC Berkeley, 210 Hearst Mining Building, Berkeley, California 94720-1760, United States

Supporting Information

ABSTRACT: The reactivity of mixtures of high voltage spinel cathode materials $Li_2NiMn_3O_8$, $Li_2FeMn_3O_8$, and $LiCoMnO_4$ cosintered with $Li_{1.5}Al_{0.5}Ti_{1.5}(PO_4)_3$ and $Li_{6.6}La_3Zr_{1.6}Ta_{0.4}O_{12}$ electrolytes is studied by thermal analysis using X-ray-diffraction and differential thermoanalysis and thermogravimetry coupled with mass spectrometry. The results are compared with predicted decomposition reactions from first-principles calculations. Decomposition of the mixtures begins at 600 °C, significantly lower than the decomposition temperature of any component, especially the electrolytes. For the cathode + $Li_{6.6}La_3Zr_{1.6}Ta_{0.4}O_{12}$ mixtures, lithium and oxygen from the electrolyte react with the cathodes to form highly stable Li_2MnO_3 and then decompose to form stable and often insulating phases such as $La_2Zr_2O_7$, La_2O_3, La_3TaO_7, TiO_2, and $LaMnO_3$ which are likely to increase the interfacial impedance of a cathode composite. The decomposition reactions are identified with high fidelity by first-principles calculations. For the cathode + $Li_{1.5}Al_{0.5}Ti_{1.5}(PO_4)_3$ mixtures, the Mn tends to oxidize to MnO_2 or Mn_2O_3, supplying lithium to the electrolyte for the formation of Li_3PO_4 and metal phosphates such as $AlPO_4$ and $LiMPO_4$ (M = Mn, Ni). The results indicate that high temperature cosintering to form dense cathode composites between spinel cathodes and oxide electrolytes will produce high impedance interfacial products, complicating solid state battery manufacturing.

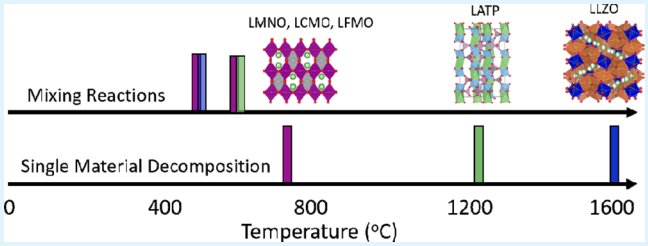

KEYWORDS: *solid ion conductor, garnet, interfacial reactivity, atomistic modeling, solid electrolyte*

INTRODUCTION

The development of lithium ion batteries has made consistent progress during the previous decades and is reaching performance and cost targets that make them attractive for emerging markets such as electric vehicles, grid storage, and wearable electronics. However, despite the advances, the ceiling of conventional lithium ion batteries is limited by the capacity of the graphitic anode and the achievable voltage and capacity limits at the positive electrode.[1,2] In order to achieve higher energy densities, new architectures must allow for high energy density anodes such as lithium metal or silicon and high voltage cathodes such as manganese spinel materials, all while improving upon the safety of lithium ion batteries.

A promising direction is to move toward the replacement of the liquid electrolyte and conventional separator with a lithium ion conducting solid forming a solid state battery.[3,4] Critical to the success of solid state batteries is the ability to form stable interfaces, impervious to reduction against lithium metal and oxidation at the cathode. When this is achieved, such as in thin film batteries with a lithium phosphorus oxynitride (LiPON) electrolyte, it is possible to demonstrate thousands of cycles using lithium metal and high voltage $LiNi_{0.5}Mn_{1.5}O_4$ cathode.[5] However, in practice, achieving this level of compatibility is difficult. Most materials have been shown to be unstable against lithium metal reduction, including the high conductivity sulfides and oxides.[6−9] In fact, even LiPON was recently shown to decompose into a stable passivation layer.[10] Similarly, prevention of the solid electrolyte toward oxidation at the positive electrode is difficult. For sulfide electrolytes, researchers tend to use an oxide coating deposited on the cathode to prevent reaction.[11−13] Although oxide electrolytes can be stable at high voltages,[14] their high conductivity is

Received: July 22, 2016
Accepted: September 19, 2016
Published: September 19, 2016

DOI: 10.1021/acsami.6b09059
ACS Appl. Mater. Interfaces 2016, 8, 26842−26850

usually achieved when the number of grain boundaries is minimized, as they can dominate the resistivity of the electrolyte.[15] Densifying oxide electrolytes often requires high temperature sintering and, in order to achieve intimate contact with the cathode, cosintering of the electrolyte and cathode into a dense pellet is necessary. This cosintering can lead to the formation of a resistive layer through interdiffusion or decomposition.[16] Identifying the decomposition reactions that occur is important to designing a solid state battery. Further, the ability to predict *a priori*, which interfacial products form, simplifies the design process. Toward this end, in this work, we show how a combination of ab initio calculations, experimental thermal analysis techniques, and X-ray-diffraction together elucidate the decomposition reactions between high voltage spinel $Li_2NiMn_3O_8$ (LNMO), $Li_2FeMn_3O_8$ (LFMO), and $LiCoMnO_4$ (LCMO) cathodes in contact with $Li_{1.5}Al_{0.5}Ti_{1.5}(PO_4)_3$ (LATP) and $Li_{6.6}La_3Zr_{1.6}Ta_{0.4}O_{12}$ (LLZ:Ta) oxide solid electrolytes during high temperature cosintering.

METHODS

Experimental Section. Spinel cathode materials, LNMO, LFMO, or LCMO, were synthesized by the Pechini method.[17] Prior to the Pechini synthesis, aqueous solutions of Li-, Ni-, Fe-, Co-, and Mn-nitrates were prepared and their cation contents were quantified by inductively coupled plasma atomic emission spectroscopy (Thermo Elemental, IRIS Intrepid). Nitrate solutions were weighed and mixed together corresponding to the desired stoichiometry of the spinel samples. Citric acid was added into an individual solution in a molar ratio of $n_{\text{citric acid}}/n_{\text{cations}} = 1.8$. The suspensions were stirred until clear solutions were obtained. 120 mL of ethylene glycol was added to each solution (corresponding to a final sample weight of 30 g). The solutions were stirred continuously and kept at 90 °C for water evaporation. The residues were heat treated at 300 °C for decomposition for several hours on heating plates. The first calcination step was at 650 °C for 5 h in a furnace. The second calcination step was completed after another 5 h at 650 °C in a muffle furnace. Afterward, the sample was ball milled in ethanol using yttria-stabilized zirconia balls and heat treated again at 650 °C for 5 h. The LATP and LLZ:Ta powders were synthesized by sol–gel and solid state reactions, respectively, described elsewhere.[18,19]

The spinels LNMO, LFMO, or LCMO were mixed with either LATP or LLZ:Ta in a volume ratio of 50:50 using a mortar and pestle, to produce "spinel + electrolyte" powders. The mixed spinel + electrolyte powders were pressed into pellets with a pressure of 370 MPa using pressing dies with 13 mm diameter. Sintering of pellets was carried out on MgO plates in corundum crucibles at 600, 700, and 800 °C for the spinel + LATP pellets and at 400, 600, and 800 °C for the spinel + LLZ:Ta pellets. Dwell time was 1 h each and heating rate was 5 K/min.

X-ray-diffraction (XRD) measurements were performed on the heat treated spinel + electrolyte pellets using a D4 ENDEAVOR (Bruker axs) with Cu Kα radiation from 10° to 80° with a 2θ step width of 0.02° and a 0.75 s accumulative time. Qualitative phase analysis was carried out on the basis of the powder diffraction file (PDF) database and the inorganic crystal structure database (ICSD, reference numbers listed in Table S1) using the software package EVA (Bruker axs). Due to the multiphase compositions of the samples and due to too many common peak positions of a series of low symmetric phases, reliable phase quantification was not attempted using Rietveld refinement.

Differential thermoanalysis and thermogravimetry coupled with mass spectroscopy (DTA/TG/MS) measurements were carried out using a NETZSCH STA 449F1 in N_2/O_2 atmosphere (technical air). Spinel powders LNMO, LFMO, and LCMO were analyzed by DTA/TG from room temperature to 1400 °C and back to room temperature at a heating and cooling rate of 10 K/min. DTA/TG was carried out from room temperature to 1200 °C and back to room temperature at a heating and cooling rate of 5 K/min on spinel + LATP mixtures. DTA/TG/MS was carried out on spinel + LLZ:Ta mixtures from room temperature to 1100 °C and back to room temperature at a heating and cooling rate of 5 K/min.

Computation. Multicomponent phase diagrams constructed with data from both density functional theory (DFT) calculations and experimental data has been shown to be useful for studying the mixing thermodynamics of solid–solid interfaces.[14] In this work, we use this approach to predict the interfacial products that form between the solid electrolyte and cathode materials upon cosintering at elevated temperatures.

To evaluate the stability of compounds, we construct grand potential phase diagrams using the pymatgen software package.[20] To obtain bulk energies, we employ DFT within the Projector Augmented Wave (PAW) formalism[21] using the generalized gradient approximation[22] to the exchange-correlation energy as implemented in the Vienna ab initio simulation package (VASP)[23] to calculate the formation energy of each compound from the nearest phases present in the NIST-JANAF[24] or Kubaschewski[25] thermochemical tables or from the elements. A cutoff energy of 520 eV and a *k*-point grid of at least $500/n_{\text{atoms}}$ was used for all calculations. The nearest phases are uniquely defined as those that define the Gibbs triangle (the low energy facet) containing the desired composition in the phase diagram. This phase diagram is generated using the DFT computed energies to determine the convex hull. The stability of the electrolytes is calculated with reference to the phase diagram hull energy at the location of the electrolyte compositions.

On the basis of the methods of Wang et al.[26] and Ong and co-workers,[27,28] the effect of temperature upon phase diagrams can be approximated by generating the oxygen grand potential phase diagrams and then mapping the oxygen chemical potential to temperature. The normalized mixing energy and the decomposition products formed at the interfaces are determined by calculating the energy at the different facets along the tie-line between cathode and electrolyte.[14,28] At a given oxygen chemical potential, the reaction energy is found by

$$\Delta E[c_a, c_b] = E_{pd}[xc_a + (1-x)c_b] - xE[c_a] - (1-x)E[c_b] \quad (1)$$

where c_a and c_b are the electrolyte and cathode compositions, respectively, and x is a mixing parameter that can vary between 0 and 1. The energies considered are the grand potential free energies after applying the external oxygen chemical potential corresponding to eq 1. The first term on the right side (E_{pd}) represents the energy of the "products" along the tie-line. The other energy terms are the grand potential energies of the end members (i.e., electrolyte and cathode). The minimum along this tie-line is considered to be the most likely reaction at a given temperature. An example is seen in Figure 1 for the reactions between spinel + LATP and spinel + LLZ:Ta at 800 °C.

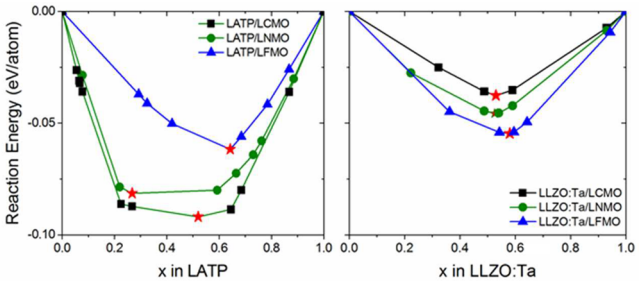

Figure 1. Mixing energy between spinel + electrolyte at 800 °C; the boundaries between facets are marked with a point, and the minimum reaction energy is the predicted reaction, denoted by the red star. The reactions are given in Table S3.

DOI: 10.1021/acsami.6b09059
ACS Appl. Mater. Interfaces 2016, 8, 26842–26850

RESULTS

Spinel Decomposition. The thermal decomposition characteristics in air of all three investigated high voltage cathodes are comparable, as shown in Figure 2. After initial

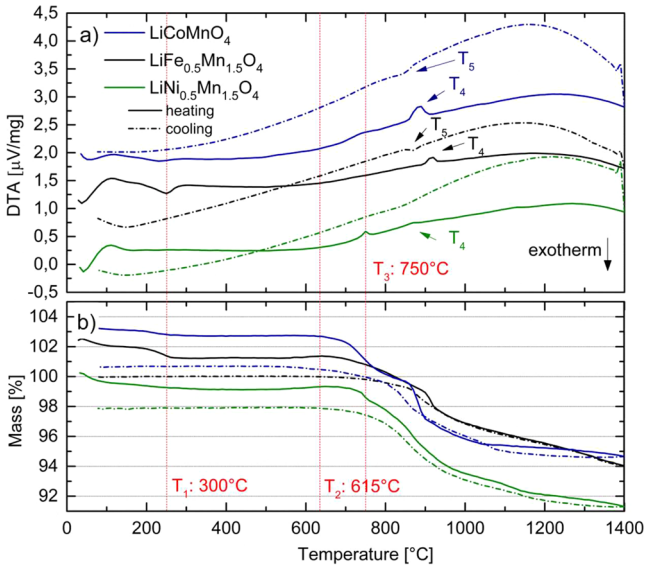

Figure 2. (a) DTA and (b) TG results of spinel powders. Experiments were carried out from room temperature to 1400 °C with a heating and cooling rate of 10 K/min. DTA signal offset: 1 unit (for LFMO); 2 units (for LCMO). TG signal offset: 2 units (for LFMO) and 4 units (for LCMO).

reactions for the desorption of surface-adsorbed H_2O below 300 °C, the TG signals remain constant and no DTA signals are observed. From T_2 = 650 °C and higher, mass loss occurs parallel to endothermic reactions at T_3 and T_4 in several steps. For both the LCMO and LNMO, a reaction takes place at T_3 = 750 °C but not for LFMO. The peak temperatures of the endothermic reactions at T_4 are slightly different for the different samples with $T_{4\_LNMO} < T_{4\_LCMO} < T_{4\_LFMO}$. During cooling, a mass uptake of around 70−80% of the lost mass between T_2 and the maximum temperature (T_{max}) is measured for all three samples. Additionally, for LFMO and LCMO, exothermic reactions are measured at temperature T_5. These results are consistent with earlier reported properties for the thermal decomposition of lithium manganese spinels.[29−32] It is known that $LiMn_2O_4$ spinels show three decomposition reactions upon heating. The first decomposition starts at around 750 °C by releasing oxygen from the lattice and formation of an oxygen defect spinel and Li_2MnO_3. Above 915 °C, as a second step, Li_2MnO_3 and spinel react to form $LiMnO_2$ while manganese is reduced and oxygen is released from the lattice.

Results from the ab initio grand potential phase diagram are in agreement with these findings. Oxygen loss and decomposition begins around 510 °C with the reactions:

$$Li_2Mn_3FeO_8 \rightarrow 0.417O_2 + Li_2MnO_3 + 0.667Mn_3O_4 + 0.50Fe_2O_3;\ \mu_O = -1.39\,eV;\ T \approx 510\,°C$$

$$\mu_O = -1.50\,eV$$

$$Li_2Mn_3NiO_8 \rightarrow 0.833O_2 + 1.0NiO + 0.333Mn_3O_4 + 2.0LiMnO_2;\ \mu_O = -1.53\,eV;\ T \approx 560\,°C$$

Decomposition of the electrolytes occurs at much higher temperatures, Figure S1. Oxygen loss from LATP is predicted to begin around 1270 °C (Table S2) with the reduction of Ti^{4+} to form $Li_2Ti_2(PO_4)_3$, $Li_4P_2O_7$, and $AlPO_4$. This is higher than the results that found LATP to be stable to 900 °C.[33] Decomposition of LLZ:Ta is calculated to occur at about 1600 °C with the reduction of Ta and the formation of La_2O_3, $Li_6Zr_2O_7$, and Li_5TaO_5.

Spinel + LLZ:TA. The thermal analysis by DTA/TG/MS of the spinel + LLZ:Ta powders reveals a comparable behavior upon heating for all three mixtures (Figure 3). Several

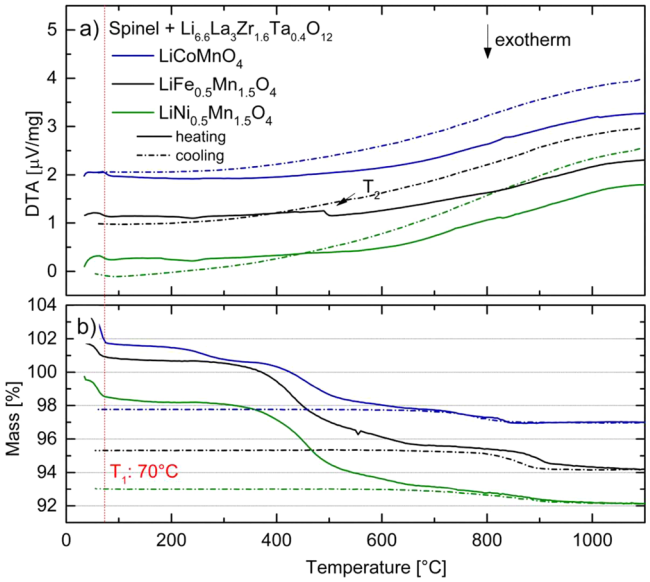

Figure 3. (a) DTA and (b) TG results of spinel + LLZ powders. Experiments were carried out from room temperature to 1100 °C with a heating and cooling rate of 5 K/min. DTA signal offset: 1 unit (for LFMO) and 2 units (for LCMO). TG signal offset: 2 units (for LFMO) and 4 units (for LCMO).

sequential mass loss steps are already observed below 500 °C, which can be assigned to the loss of CO_2 and H_2O by MS (not shown). The loss of CO_2 and H_2O at temperatures below 600 °C is characteristic for air sensitive LLZ:Ta.[34] No significant endo- or exothermic reactions can be observed within the whole measured temperature range. A small endothermic signal is detected for LFMO + LLZ:Ta at 490 °C. Nevertheless, mass loss continues above 600 °C, but no elements were detected by MS. Between T_1 and T_{max}, around 6.5 wt % mass is released from the LFMO + LLZ:Ta sample, 6.0 wt % from the LNMO + LLZ:Ta sample, and 4.5 wt % from the LMCO + LLZ:Ta sample, whereas around 13−17% of this mass is taken up again during cooling.

XRD performed on spinel + LLZ:Ta pellets that were heat treated at 400, 600, and 800 °C showed major phase changes starting at 600 °C, Figures 4−6. The evolution of phase content from 400 to 800 °C is comparable for all three mixtures. For the sample heat treated at 400 °C, the observed diffraction pattern is the same as the diffraction pattern of the as-mixed powders. Only LLZ:Ta and spinel (here described by a $LiMn_2O_4$ phase with adjusted lattice parameter a = 8.06

DOI: 10.1021/acsami.6b09059
ACS Appl. Mater. Interfaces 2016, 8, 26842−26850

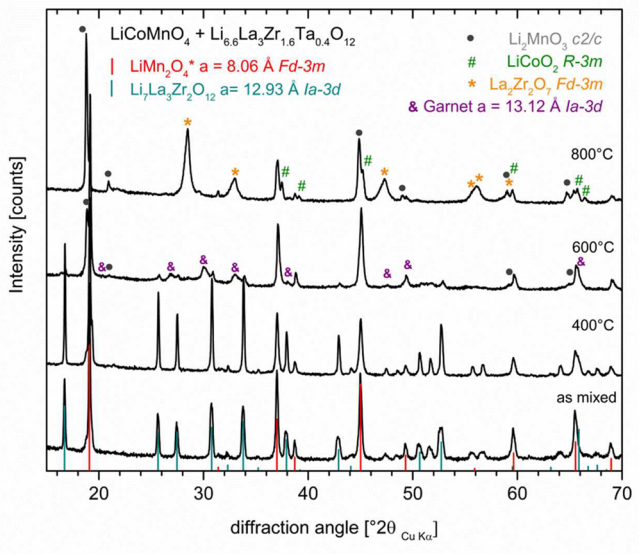

Figure 4. XRD patterns of LCMO + LLZ:Ta mixtures that were heat treated at 800, 600, and 400 °C and as mixed powder. Table S3 lists the consulted reference patterns.

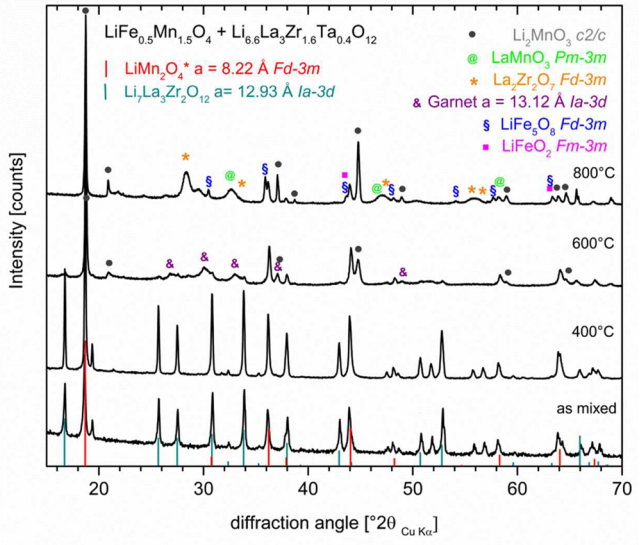

Figure 5. XRD patterns of LFMO + LLZ:Ta mixtures that were heat treated at 800, 600, and 400 °C and as mixed powder. Table S3 lists the consulted reference patterns.

according to ref 35) can be detected. The XRD pattern for the spinel + LLZ:Ta pellet which was heat treated at 600 °C shows a contribution of spinel and LLZ:Ta but a significant decrease in diffraction peak intensities of the LLZ:Ta phase in comparison with the diffraction pattern of the as mixed sample. Additionally, the pattern includes a secondary garnet phase and monoclinic Li_2MnO_3. The decomposition of lithium manganese spinels to Li_2MnO_3 usually occurs at temperatures around 750 °C.[29,31,32] The detection of larger quantities of Li_2MnO_3, as was shown here, therefore indicates an accelerated formation of Li_2MnO_3 at lower temperatures due to Li supply and oxygen uptake from LLZ:Ta. Accordingly, a low amount of LLZ:Ta was detected as well as a secondary garnet phase that very likely exhibits a Li-depleted stoichiometry.

For the samples heat treated at 800 °C, the peak intensities of the spinel phases are decreased and no more LLZ:Ta can be

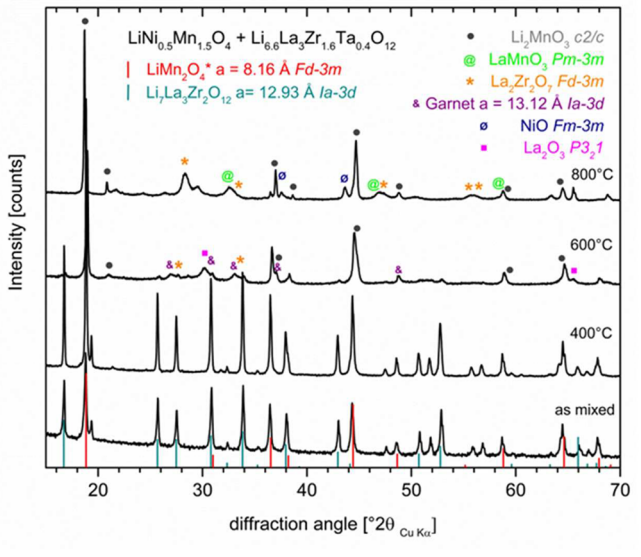

Figure 6. XRD patterns of LNMO + LLZ:Ta mixtures that were heat treated at 800, 600, and 400 °C and as mixed powder. Table S3 lists the consulted reference patterns.

detected. Instead, a $La_2Zr_2O_7$ phase can be identified clearly. Additionally, for LCMO, Li_2MnO_3 and $LiCoO_2$ are found. For the LFMO + LLZ:Ta sample, $LaMnO_3$ and $LiFe_5O_8$ are also found, whereas $LaMnO_3$ and NiO is found in the LNMO + LLZ:Ta sample.

XRD results from the spinel + LLZ:Ta samples indicated the formation of new phases from at least 600 °C. Since these new phases are stable upon cooling to room temperature, the decomposition products will affect the interfacial properties of an assembled composite cathode in a solid state battery.

Spinel + LATP. Figure 7 shows the DTA/TG results of the spinel + LATP powders. The characteristics upon heating to 1200 °C of all three mixtures are comparable. An initial mass

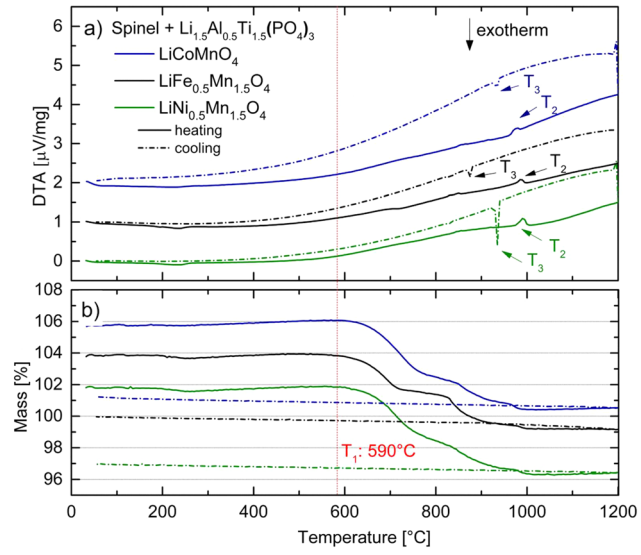

Figure 7. (a) DTA and (b) TG of spinel + LATP powders. Experiments were carried out from room temperature to 1200 °C at a heating and cooling rate of 5 K/min. DTA signal offset: 1 unit (for LFMO) and 2 units (for LCMO). TG signal offset: 2 units (for LFMO) and 4 units (for LCMO).

DOI: 10.1021/acsami.6b09059
ACS Appl. Mater. Interfaces 2016, 8, 26842−26850

loss due to the release of surface-adsorbed H_2O and CO_2 occurs below 270 °C = T_1. A continuous mass loss starting at T_3 is very small for all three mixtures and occurs at around 860 °C, whereas T_4 lies at 980 °C for LCMO + LATP and slightly higher, at 990 °C, for the other two mixtures. A mass loss of around 5−6 wt % can be measured for all three samples from T_2 to T_{max}. Around 15% of the lost mass is taken up again during cooling. Additionally, an exothermic reaction was measured during cooling for LCMO + LATP and LFMO + LATP at around 935 and 930 °C, respectively, and for LNMO + LATP at around 880 °C. The products of the spinel + LATP reaction upon heating showed a significantly lower amount of mass uptake during cooling than the single spinel materials. A reversible mass uptake is very characteristic for lithium manganese spinels,[29] thus proposing that the lithium manganese spinel phase almost completely is transformed into new phases by the reaction with LATP at maximal temperature of 1200 °C.

XRD performed on LCMO + LATP pellets which were heat treated at 600, 700, and 800 °C are shown in Figure 8. The

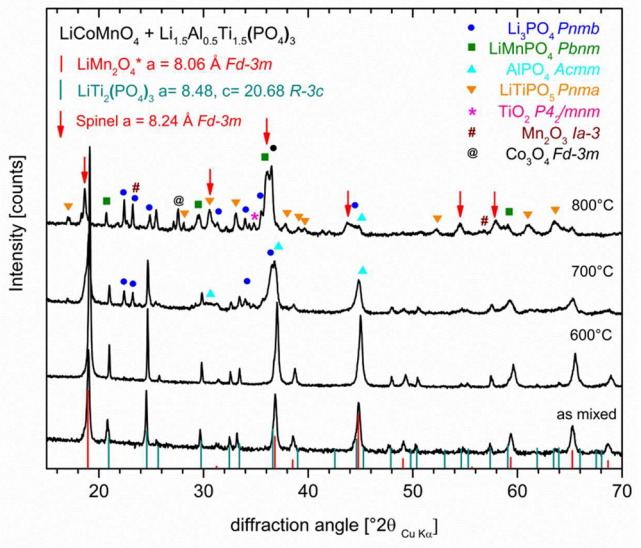

Figure 8. XRD patterns of LCMO + LATP mixtures that were heat treated at 800, 700, and 600 °C and as mixed powder. Table S3 lists the consulted reference patterns.

XRD pattern for the LATP + LCMO pellet heat treated at 600 °C is described sufficiently by a spinel phase with a cubic lattice parameter of a = 8.06 Å[35] and LATP, which is described by a $LiTi_2(PO_4)_3$ phase with a = 8.47 Å and c = 20.87 Å. Major changes are seen at 700 °C; both original phases were detected at their initial peak positions, but the intensities of the $LiTi_2(PO_4)_3$ and $LiMn_2O_4$ phase decrease significantly when compared with the sample heat treated at 600 °C. Additionally, the pattern needs to be described by at least two orthorhombic phosphate phases and TiO_2 which indicates that the mixture of LATP and LCMO already has serious chemical reaction at this temperature. At 800 °C, LATP is consumed completely by forming new phosphate phases in reaction with LCMO. Accordingly, a significant peak shift of the spinel phase toward lower angles at 800 °C indicates a lattice expansion and a major change in chemistry. Additionally, a series of orthorhombic phosphates is necessary to describe the observed patterns completely. Furthermore, TiO_2, Mn_2O_3, and Co_3O_4 can be detected.

Similar observations were made for LNMO + LATP by XRD analysis as shown in Figure 9. The XRD pattern for the LNMO

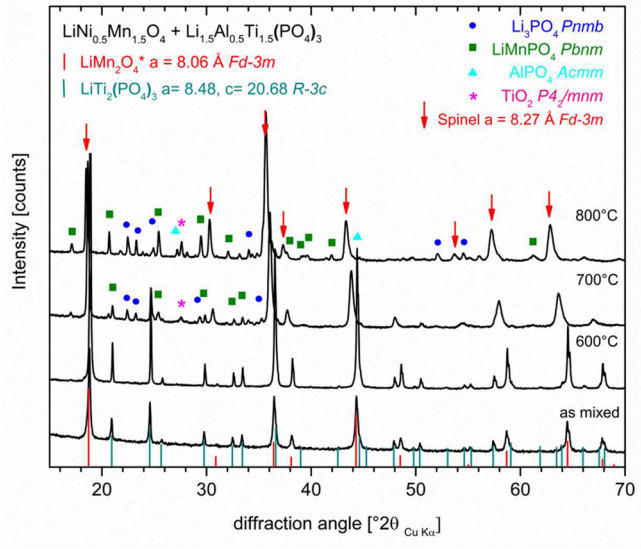

Figure 9. XRD patterns of LNMO + LATP mixtures that were heat treated at 800, 700, and 600 °C and as mixed powder. Table S3 lists the consulted reference patterns.

+ LATP pellet heat treated at 600 °C is described completely by a $LiMn_2O_4$ spinel phase with a cubic lattice parameter of a = 8.16 Å, representative for LNMO,[26] and a $LiTi_2(PO_4)_3$ phase. The intensities of the $LiTi_2(PO_4)_3$ and $LiMn_2O_4$ phases decrease significantly for the sample heat treated at 700 °C in comparison with those at 600 °C. Additionally, a tetragonal phosphate phase and rutile can be identified. Therefore, the LNMO + LATP reaction at 700 °C majorly affects the chemistry of the LNMO phase, since LNMO components react with LATP to form new phosphate phases. For the sample heat treated at 800 °C, no more LATP can be detected. The peak positions of the $LiMn_2O_4$ phase are shifted significantly to lower angles and need to be described by another spinel phase with a = 8.27 Å. A series of tetragonal phosphates is also necessary to describe the observed diffraction pattern.

For the LFMO + LATP pellet heat treated at 600 °C, two phases are detected by XRD (Figure 10). The first one is $LiMn_2O_4$ with a = 8.26 Å, representative for LFMO,[35] and the second one is LATP. For the sample heat treated at 700 °C, LFMO can still be detected but intensities are decreased, whereas LATP cannot be identified anymore. The cathode and electrolyte have almost completely reacted to form a $MnFeO_3$-like phase and orthorhombic phosphates, which occurs at a lower temperature than for the other two cathode materials. Neither LFMO nor LATP can be identified for the sample heat treated at 800 °C. Instead, at both temperatures, $MnFeO_3$ emerges as the main phase and a series of secondary tetragonal phosphates are necessary to describe the pattern satisfactorily. The $MnFeO_3$-like phase is still the main phase indicating its dominant thermodynamic stability in the LATP + LFMO pseudobinary system at 700 °C as well as at 800 °C.

The composite mixtures of spinel + LATP react strongly with each other from at least 700 °C, and similar to the spinel + LLZO:Ta composites, the decomposition products are stabilized at room temperature. The large amount of $AlPO_4$

DOI: 10.1021/acsami.6b09059
ACS Appl. Mater. Interfaces 2016, 8, 26842−26850

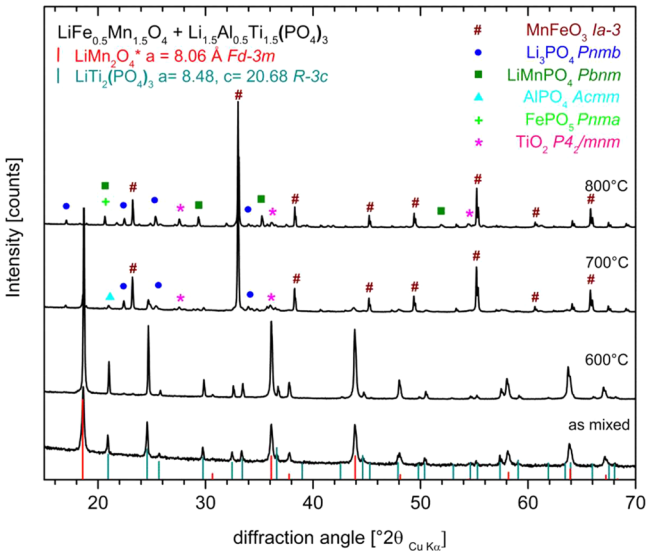

Figure 10. XRD patterns of LFMO + LATP mixtures that were heat treated at 800, 700, and 600 °C and as mixed powder. Table S3 lists the consulted reference patterns.

and Li_3PO_4 present after heat treatment will likely affect the performance of a composite cathode in a solid state battery.

Predicted Decomposition Reactions. Mixing of the oxide electrolytes and spinel cathodes results in decompositions occurring at a temperature lower than what is observed for each separate phase. This can be rationalized by following the highly mobile lithium and oxygen species. The result of mixing the spinel cathodes with LLZ:Ta is that the decomposition of the cathodes acts as an oxidizer for the decomposition of LLZ:Ta. The predicted reactions are listed in Table 1 and appear to identify the correct reactions although some of the minority phases predicted could not be detected with XRD. The decomposition of LLZ:Ta is predicted to occur around 1600 °C when heated by itself; however, in the presence of the cathodes, decomposition reactions are predicted to occur at the onset of cathode decomposition. As was pointed out in recent theoretical work, the barrier for gaseous oxygen loss from solid ceramics is rather high, and thus, decomposition can be kinetically limited.[36] When the two ceramics are in contact at elevated temperatures, however, oxygen and lithium exchange readily occur leading to decomposition. In these spinel based systems, the decomposition reactions are dominated by the formation of the highly stable Li_2MnO_3. From an analysis of the reaction products, it appears that oxygen lost from the cathode is absorbed by the LLZ:Ta electrolyte to form a lithium oxide compound which then drives the formation of Li_2MnO_3. A similar reaction likely forms $LiCoO_2$ and $LiFeO_2$ in LCMO and LFMO, respectively, while in the LNMO a reduced Ni is likely formed such as NiO.

The mixing reactions between spinel + LATP are considerably more complicated than with LLZ:Ta. There is significant mixing predicted to occur for temperatures above ~150 °C. The spinel + LATP decomposition products include Li_3PO_4 and TiO_2 formed from the decomposed LATP, as well as mixed products such as $LiMnPO_4$ in the LNMO and LFMO decomposition products. Unlike for the spinel + LLZ:Ta systems, the predicted reactions with the LATP electrolyte at experimental temperatures do not align with the experimental results. In all cases, the experimental results align best with predicted reactions at lower temperatures, Table 2. The two most likely explanations are that either the products are diffusion limited so that the formation of mixed metal compounds does not readily occur or our predictions of the most stable compounds are slightly off. For example, the

Table 1. LLZ/Cathode Reactions

		Reactions with minimum reaction energy of LLZ:Ta with:
LCMO:	600°C	$11.6Li_{6.6}La_3Zr_{1.6}Ta_{0.4}O_{12} + 39.9LiMnCoO_4 \rightarrow 0.25O_2 + La_2MnCoO_6 + 0.2La_2O_3 + 9.3La_2Zr_2O_7 + 4.7La_3TaO_7 + 38.9Li_2MnO_3 + 38.9LiCoO_2$
	800°C	$11.6Li_{6.6}La_3Zr_{1.6}Ta_{0.4}O_{12} + 39.9LiMnCoO_4 \rightarrow 0.25O_2 + La_2MnCoO_6 + 0.2La_2O_3 + 9.3La_2Zr_2O_7 + 4.7La_3TaO_7 + 38.9Li_2MnO_3 + 38.9LiCoO_2$
LNMO:	600°C	$36.9Li_{6.6}La_3Zr_{1.6}Ta_{0.4}O_{12} + 61.3Li_2Mn_3NiO_8 \rightarrow 0.25O_2 + 3.2La_2O_3 + 29.5La_2Zr_2O_7 + 14.7La_3TaO_7 + LaMnO_3 + 182.9Li_2MnO_3 + 61.3NiO$
	800°C	$5.0Li_{6.6}La_3Zr_{1.6}Ta_{0.4}O_{12} + 8.8Li_2Mn_3NiO_8 \rightarrow 4.66O_2 + 4.0La_2Zr_2O_7 + 2.0La_3TaO_7 + 25.4Li_2MnO_3 + LaMnO_3 + 8.8Ni$
LFMO:	600°C	$5.3Li_{6.6}La_3Zr_{1.6}Ta_{0.4}O_{12} + 7.25Li_2Mn_3FeO_8 + 1.8O_2 \rightarrow 4.3La_2Zr_2O_7 + 2.1La_3TaO_7 + LaFeO_3 + 21.8Li_2MnO_3 + 6.25LiFeO_2$
	800°C	$5.0Li_{6.6}La_3Zr_{1.6}Ta_{0.4}O_{12} + 7.0Li_2Mn_3FeO_8 + 1.5O_2 \rightarrow 4.0La_2Zr_2O_7 + 2.0La_3TaO_7 + LaMnO_3 + 20.0Li_2MnO_3 + 7.0LiFeO_2$

[a]Red phases were detected by XRD; blue phases were possibly detected, but their peaks overlap with other phases.

DOI: 10.1021/acsami.6b09059
ACS Appl. Mater. Interfaces 2016, 8, 26842−26850

Table 2. Spinel + LATP Reactions Which Best Match the Phases Found in XRD

		Reactions with minimum reaction energy of LATP with:
LCMO	700°C (160°C)	$2Li_{1.5}Al_{0.5}Ti_{1.5}(PO_4)_3 + 6.05LiMnCoO_4 \rightarrow 0.5O_2 + 2.0Li_3PO_4 + AlPO_4 + 3.0LiTiPO_5 + 6.02MnO_2 + 2.0Co_3O_4 + 0.02Li_2MnCo_3O_8$
	800°C (280°C)	$2Li_{1.5}Al_{0.5}Ti_{1.5}(PO_4)_3 + 6.05LiMnCoO_4 \rightarrow 0.5O_2 + 2.02Li_3PO_4 + AlPO_4 + 2.98LiTiPO_5 + 0.02TiO_2 + 6.05MnO_2 + 2.01Co_3O_4$
LNMO	700°C (360°C)	$9.73Li_{1.5}Al_{0.5}Ti_{1.5}(PO_4)_3 + 5.86Li_2Mn3NiO_8 \rightarrow 8.8O_2 + Li_3PO_4 + 4.86AlPO_4 + 17.46LiMnPO_4 + 14.59TiO_2 + 5.86LiNiPO_4 + 0.07Mn_2O_3$
	800°C (500°C)	$71.72Li_{1.5}Al_{0.5}Ti_{1.5}(PO_4)_3 + 43.23Li_2Mn3NiO_8 \rightarrow +64.9O_2 + 7.37Li_3PO_4 + 35.86AlPO_4 + 129.7LiMnPO_4 + 106.6TiO_2 + 42.2LiNiPO_4 + TiNiO_3$
LFMO	700°C (350°C)	$2.0Li_{1.5}Al_{0.5}Ti_{1.5}(PO_4)_3 + 5.93Li_2Mn_3FeO_8 \rightarrow 3.0O_2 + AlPO_4 + 0.02Li_3Fe_2(PO_4)_3 + 4.93Li_3PO_4 + 5.96Mn_2O_3 + 5.89MnFeO_3 + 3.0TiO_2$
	800°C (450°C)	$29.9Li_{1.5}Al_{0.5}Ti_{1.5}(PO_4)_3 + 88.6Li_2Mn_3FeO_8 \rightarrow 44.5O_2 + 14.9AlPO_4 + 73.7Li_3PO_4 + LiMnPO_4 + 88.1Mn_2O_3 + 88.6MnFeO_3 + 44.8TiO_2$

[a]Red phases were detected by XRD; blue phases were possibly detected, but their peaks overlap with other phases. The temperature in parentheses is the reaction temperature according to calculations.

transition between the compounds with different oxidation states, such as CoO/Co_3O_4 and MnO_2/Mn_3O_4, and the stable phosphates, $AlPO_4$, $LiMnPO_4$, and $LiCoPO_4$, have a large effect on which reactions are predicted to occur. Getting this redox equilibrium simultaneously correct in varying chemical environments is a known challenge in ab initio calculations.[27] Although beyond the scope of this work, repeating the tests with in situ XRD would further elucidate the reaction mechanisms. The reactions predicted at the experimental temperatures are shown in Table S3. An example of the oxygen transfer in the LCMO + LATP follows the reaction scheme:

$$6.05LiMnCoO_4 \rightarrow 2.01O_2 + 2.01Co_3O_4 + 6.05LiMnO_2 \quad (2)$$

$$2.51O_2 + 2.01Co_3O_4 + 6.05LiMnO_2 + 2Li_{1.5}Al_{0.5}Ti_{1.5}(PO_4)_3 \rightarrow 2.02Li_3PO_4 + AlPO_4 + 2.98LiTiPO_5 + 0.02TiO_2 + 6.05MnO_2 + 2.01Co_3O_4 \quad (3)$$

From eqs 2 and 3, we see the decomposition of LCMO followed by the oxidation of $LiMnO_2$, which then supplies lithium to react with the LATP to form MnO_2 and $LiTiPO_5$, Li_3PO_4, and $AlPO_4$ respectively. Unlike with the LLZ:Ta, in the spinel + LATP system, the decomposition products of the spinel have a strong mixing energy with the LATP suggesting that the components will mix rather than simply decompose.

In a battery, a cathode composite layer is necessary which has interpenetrating electrically and ionically conductive networks that percolate through the composite layer. It is critical that the interfaces between the ionically conductive electrolyte and the cathode active material have low resistance. Although LLZ:Ta is likely stable at high voltages,[37] troublingly, the majority of the components formed by the decomposition reactions of spinel + LLZ:Ta are insulating phases such as $La_2Zr_2O_7$, La_2O_3, La_3TaO_7, TiO_2, and $LaMnO_3$ that will likely only serve to increase the interfacial impedance. On the other hand, LCMO is predicted to form the active material $LiCoO_2$, suggesting the latter is stable at these temperatures. This is in agreement with earlier work suggesting that $LiCoO_2$ may be a better choice for a cosintered active material than the other spinels for use with LLZ:Ta.[38,39]

The large reactivity between the spinels and LATP at even modest temperatures suggest that cosintering will be difficult, especially when there are very stable products such as Li_2MnO_3 or Li_3PO_4. This is unfortunate since it is predicted that LATP is stable up to high voltages, enabling the use of high voltage cathodes.[14] Encouragingly, the decomposition products include Li_3PO_4, which has modest ionic conductivity and may allow the battery to function. Therefore, a low temperature processing route to form well-bonded composites will likely be necessary to fabricate solid state cathodes in future solid state batteries.

CONCLUSIONS

Single spinel materials as well as spinel materials in combination with the LATP or LLZ:Ta electrolyte showed thermal decomposition at temperatures above 550−600 °C. Our results show the reaction reversibility of the single spinel materials is significantly altered if mixed with either LATP or LLZ:Ta electrolyte. XRD studies revealed that spinel + LATP mixtures are compatible with each other at 600 °C for the given sintering conditions. At higher temperatures, the materials react to form new phases. Spinel + LLZ:Ta were shown not to be compatible with each other even at 600 °C. The reaction products from these decomposition reactions were predicted from first-principles phase diagrams. The results suggest that insulating phases form above 600 °C which will likely add to the interfacial impedance of composite cathode in solid state batteries.

ASSOCIATED CONTENT

Supporting Information

The Supporting Information is available free of charge on the ACS Publications website at DOI: 10.1021/acsami.6b09059.

DTA/TG data for LLZ and LATP powders, oxygen evolution profiles, and reaction energies for the mixed cathode-electrolyte systems (PDF)

DOI: 10.1021/acsami.6b09059
ACS Appl. Mater. Interfaces 2016, 8, 26842−26850

AUTHOR INFORMATION

Corresponding Author

*E-mail: Lincoln.m@samsung.com.

Notes

The authors declare no competing financial interest.

ACKNOWLEDGMENTS

The authors thank the Samsung Advanced Institute of Technology for their funding of this research. This work used the Extreme Science and Engineering Discovery Environment (XSEDE), which is supported by National Science Foundation grant number ACI-1053575. A.W. gratefully acknowledges financial support by "Bundesministerium für Bildung und Forschung" (Federal ministry of education and research), Germany, under project no. 03SF0477A. Financial support for Q.M. by the "Initiative and Networking Fund" of Helmholtz-Gemeinschaft Deutscher Forschungszentren e.V. in the framework of the Helmholtz Energieallianz "Stationäre elektrochemische Feststoffspeicher und -wandler" (HA-E-0002) is gratefully acknowledged. S.U. and C.-L.T. received funding from Helmholtz-Gemeinschaft Deutscher Forschungszentren e.V. under grant "Elektrochemische Speicher im System −Zuverlässigkeit und Integration" under support code PoF2-REUN. C.-L.T., S.U., Q.M., and O.G. received funding from Helmholtz-Gemeinschaft Deutscher Forschungszentren e.V. under grant "Speicher und vernetzte Infrastrukturen" under support code PoF3-SCI. The authors thank M.-T. Gerhards, Institute of Energy and Climate Research IEK-1: Materials Synthesis and Processing (IEK-1), Forschungszentrum Jülich GmbH, for the DTA/TG/MS measurements as well as Sabrina Tückhardt and Jennifer Pelikan, Central Institute for Engineering, Electronics and Analytics (ZEA-3), Forschungszentrum Jülich GmbH, for the ICP-OES measurements.

REFERENCES

(1) Thackeray, M. M.; Wolverton, C.; Isaacs, E. D. Electrical Energy Storage for Transportation—approaching the Limits Of, and Going Beyond, Lithium-Ion Batteries. *Energy Environ. Sci.* **2012**, *5* (7), 7854−7863.

(2) Manthiram, A. Materials Challenges and Opportunities of Lithium Ion Batteries. *J. Phys. Chem. Lett.* **2011**, *2* (3), 176−184.

(3) Dudney, N. J. Solid-State Thin-Film Rechargeable Batteries. *Mater. Sci. Eng., B* **2005**, *116* (3), 245−249.

(4) Hayashi, A.; Tatsumisago, M. Invited Paper: Recent Development of Bulk-Type Solid-State Rechargeable Lithium Batteries with Sulfide Glass-Ceramic Electrolytes. *Electron. Mater. Lett.* **2012**, *8* (2), 199−207.

(5) Li, J.; Ma, C.; Chi, M.; Liang, C.; Dudney, N. J. Solid Electrolyte: The Key for High-Voltage Lithium Batteries. *Adv. Energy Mater.* **2015**, *5* (4), 1401408.

(6) Haruyama, J.; Sodeyama, K.; Han, L.; Takada, K.; Tateyama, Y. Space-Charge Layer Effect at Interface between Oxide Cathode and Sulfide Electrolyte in All-Solid-State Lithium-Ion Battery. *Chem. Mater.* **2014**, *26* (14), 4248−4255.

(7) Kim, K. H.; Iriyama, Y.; Yamamoto, K.; Kumazaki, S.; Asaka, T.; Tanabe, K.; Fisher, C. A. J.; Hirayama, T.; Murugan, R.; Ogumi, Z. Characterization of the Interface between $LiCoO_2$ and $Li_7La_3Zr_2O_{12}$ in an All-Solid-State Rechargeable Lithium Battery. *J. Power Sources* **2011**, *196* (2), 764−767.

(8) Ong, S. P.; Mo, Y.; Richards, W. D.; Miara, L.; Lee, H. S.; Ceder, G. Phase Stability, Electrochemical Stability and Ionic Conductivity of the $Li_{10\pm1}MP_2X_{12}$ (M = Ge, Si, Sn, Al or P, and X = O, S or Se) Family of Superionic Conductors. *Energy Environ. Sci.* **2013**, *6* (1), 148.

(9) Wenzel, S.; Randau, S.; Leichtweiß, T.; Weber, D. A.; Sann, J.; Zeier, W. G.; Janek, J. Direct Observation of the Interfacial Instability of the Fast Ionic Conductor Li10GeP2S12 at the Lithium Metal Anode. *Chem. Mater.* **2016**, *28* (7), 2400−2407.

(10) Schwöbel, A.; Hausbrand, R.; Jaegermann, W. Interface Reactions between LiPON and Lithium Studied by in-Situ X-Ray Photoemission. *Solid State Ionics* **2015**, *273*, 51−54.

(11) Ohta, N.; Takada, K.; Sakaguchi, I.; Zhang, L.; Ma, R.; Fukuda, K.; Osada, M.; Sasaki, T. $LiNbO_3$-Coated $LiCoO_2$ as Cathode Material for All Solid-State Lithium Secondary Batteries. *Electrochem. Commun.* **2007**, *9* (7), 1486−1490.

(12) Nagao, M.; Hayashi, A.; Tatsumisago, M. Fabrication of Favorable Interface between Sulfide Solid Electrolyte and Li Metal Electrode for Bulk-Type Solid-State Li/S Battery. *Electrochem. Commun.* **2012**, *22*, 177−180.

(13) Kamaya, N.; Homma, K.; Yamakawa, Y.; Hirayama, M.; Kanno, R.; Yonemura, M.; Kamiyama, T.; Kato, Y.; Hama, S.; Kawamoto, K.; Mitsui, A. A Lithium Superionic Conductor. *Nat. Mater.* **2011**, *10* (9), 682−686.

(14) Richards, W. D.; Miara, L. J.; Wang, Y.; Kim, J. C.; Ceder, G. Interface Stability in Solid-State Batteries. *Chem. Mater.* **2016**, *28* (1), 266−273.

(15) Fergus, J. W. Ceramic and Polymeric Solid Electrolytes for Lithium-Ion Batteries. *J. Power Sources* **2010**, *195* (15), 4554−4569.

(16) Luntz, A. C.; Voss, J.; Reuter, K. Interfacial Challenges in Solid-State Li Ion Batteries. *J. Phys. Chem. Lett.* **2015**, *6* (22), 4599−4604.

(17) Pechini, M. P. Method of Preparing Lead and Alkaline Earth Titanates and Niobate and Coating Method Using the Same To Form a Capacitor. Patent US3330697A, 1967.

(18) Ma, Q.; Xu, Q.; Tsai, C. L.; Tietz, F.; Guillon, O. A Novel Sol-Gel Method for Large-Scale Production of Nanopowders: Preparation of Li1.5Al0.5Ti1.5(PO4)3 as an Example. *J. Am. Ceram. Soc.* **2016**, *99* (2), 410−414.

(19) Tsai, C.-L.; Roddatis, V.; Chandran, C. V.; Ma, Q.; Uhlenbruck, S.; Bram, M.; Heitjans, P.; Guillon, O. Li7La3Zr2O12 Interface Modification for Li-Dendrite Prevention. *ACS Appl. Mater. Interfaces* **2016**, *8* (16), 10617−10626.

(20) Ong, S. P.; Richards, W. D.; Jain, A.; Hautier, G.; Kocher, M.; Cholia, S.; Gunter, D.; Chevrier, V. L.; Persson, K. a.; Ceder, G. Python Materials Genomics (Pymatgen): A Robust, Open-Source Python Library for Materials Analysis. *Comput. Mater. Sci.* **2013**, *68*, 314−319.

(21) Blöchl, P. E. Projector Augmented-Wave Method. *Phys. Rev. B: Condens. Matter Mater. Phys.* **1994**, *50* (24), 17953−17979.

(22) Perdew, J. P.; Burke, K.; Ernzerhof, M. Generalized Gradient Approximation Made Simple. *Phys. Rev. Lett.* **1996**, *77* (18), 3865−3868.

(23) Kresse, G.; Furthmüller, J. Efficient Iterative Schemes for Ab Initio Total-Energy Calculations Using a Plane-Wave Basis Set. *Phys. Rev. B: Condens. Matter Mater. Phys.* **1996**, *54* (16), 11169−11186.

(24) Chase, M. *NIST-JANAF Thermochemical Tables*; American Chemical Society; American Institute of Physics for the National Institute of Standards and Technology: Washington D.C.; Woodbury N.Y., 1998.

(25) Kubaschewski, O. *Materials Thermochemistry*; Pergamon Press: Oxford, 1993.

(26) Wang, L.; Maxisch, T.; Ceder, G. A First-Principles Approach to Studying the Thermal Stability of Oxide Cathode Materials. *Chem. Mater.* **2007**, *19* (3), 543−552.

(27) Ong, S. P.; Wang, L.; Kang, B.; Ceder, G. Li−Fe−P−O 2 Phase Diagram from First Principles Calculations. *Chem. Mater.* **2008**, *20* (5), 1798−1807.

(28) Huang, Y.; Lin, Y.-C.; Jenkins, D. M.; Chernova, N. A.; Chung, Y.; Radhakrishnan, B.; Chu, I.-H.; Fang, J.; Wang, Q.; Omenya, F.; Ong, S. P.; Whittingham, M. S. Thermal Stability and Reactivity of Cathode Materials for Li-Ion Batteries. *ACS Appl. Mater. Interfaces* **2016**, *8* (11), 7013−7021.

(29) Thackeray, M. M.; Mansuetto, M. F.; Dees, D. W.; Vissers, D. R. The Thermal Stability of Lithium-Manganese-Oxide Spinel Phases. *Mater. Res. Bull.* **1996**, *31* (2), 133−140.

DOI: 10.1021/acsami.6b09059
ACS Appl. Mater. Interfaces 2016, 8, 26842−26850

(30) Cupid, D. M.; Reif, A.; Seifert, H. J. Enthalpy of Formation of Li1+xMn2-xO4 (0 < X < 0.1) Spinel Phases. *Thermochim. Acta* **2015**, *599*, 35−41.
(31) Yamaguchi, R.; Ikuta, H.; Wakihara, M. Heat of Formation for LiMyMn2−yO4 (M = Co, Cr, Li, Mg, Ni) Spinel Solid Solution. *J. Therm. Anal. Calorim.* **1999**, *57* (3), 797−806.
(32) Mandal, S.; Rojas, R. M.; Amarilla, J. M.; Calle, P.; Kosova, N. V.; Anufrienko, V. F.; Rojo, J. M. High Temperature Co-Doped LiMn2O4 -Based Spinels. Structural, Electrical, and Electrochemical Characterization. *Chem. Mater.* **2002**, *14* (4), 1598−1605.
(33) Narváez-Semanate, J. L.; Rodrigues, A. C. M. Microstructure and Ionic Conductivity of Li1+xAlxTi2−x(PO4)3 NASICON Glass-Ceramics. *Solid State Ionics* **2010**, *181* (25), 1197−1204.
(34) Wang, Y.; Lai, W. Phase Transition in Lithium Garnet Oxide Ionic Conductors Li7La3Zr2O12: The Role of Ta Substitution and H2O/CO2 Exposure. *J. Power Sources* **2015**, *275*, 612−620.
(35) Kawai, H.; Nagata, M.; Kageyama, H.; Tukamoto, H.; West, A. R. 5 V Lithium Cathodes Based on Spinel Solid Solutions Li2Co1+XMn3−XO8: −1 ≤ X ≤ 1. *Electrochim. Acta* **1999**, *45* (1−2), 315−327.
(36) Zhu, Y.; He, X.; Mo, Y. First Principles Study on Electrochemical and Chemical Stability of the Solid Electrolyte-Electrode Interfaces in All-Solid-State Li-Ion Batteries. *J. Mater. Chem. A* **2016**, *4* (9), 3253−3266.
(37) Tsai, C.-L.; Dashjav, E.; Hammer, E.-M.; Finsterbusch, M.; Tietz, F.; Uhlenbruck, S.; Buchkremer, H. P. High Conductivity of Mixed Phase Al-Substituted Li7La3Zr2O12. *J. Electroceram.* **2015**, *35* (1−4), 25−32.
(38) Miara, L. J.; Richards, W. D.; Wang, Y. E.; Ceder, G. First-Principles Studies on Cation Dopants and Electrolyte|Cathode Interphases for Lithium Garnets. *Chem. Mater.* **2015**, *27* (11), 4040−4047.
(39) Ren, Y.; Liu, T.; Shen, Y.; Lin, Y.; Nan, C.-W. Chemical Compatibility between Garnet-like Solid State Electrolyte Li6.75-La3Zr1.75Ta0.25O12 and Major Commercial Lithium Battery Cathode Materials. *J. Mater.* **2016**, *2* (3), 256−264.

DOI: 10.1021/acsami.6b09059
ACS Appl. Mater. Interfaces 2016, 8, 26842−26850